

Robust and Expedited Methodologies for Resolving Radiation View Factors

Natan P. Herzog

Eliana M. Crew

Shane P. Riley

Matthew M. Barry

Abstract

The effects of mesh refinement using the distmesh2d algorithm and gaussian integration on the numerical accuracy of the Double Area Integration (DAI) and Single Area Integration (SAI) numerical methods for evaluating the view factor between two surfaces were studied. It was determined that SAI presents an advantage in eliminating the need for mesh refinement of the receiving surface. Gaussian integration proved to dramatically increase numerical accuracy by, in some cases, five orders of magnitude. These results were applied to the evaluation of view factors for the hot shoe array within a General Purpose Heat Source RTG. It was found that the top and bottom rows are dramatically worse-performing than the remaining rows and that the columns facing the corner of the fuel stack have significantly lower view factors than the others.

Robust and Expedited Methodologies for Resolving Radiation View Factors

1 Introduction

Radioisotope thermoelectric generators (RTGs) are used to produce electricity for space missions where harnessing the sun's energy is practically impossible. RTGs have been in use by the National Aeronautics and Space Administration (NASA) for such missions since 1961, when the Transit IV-A mission launched [1]. They continue to be among the most reliable devices for such contexts. However, as the power requirements of modern space missions increase, it becomes ever more imperative to characterize a mission's power capabilities before launch, at which point it will become inaccessible for maintenance.

The theoretical maximum efficiency, η_{carnot} , of an engine in converting heat into useful work is given by

$$\eta_{\text{carnot}} = 1 - \frac{T_L}{T_H} \quad (1)$$

where T_H and T_L are the hot- and cold-side reservoir temperatures for the engine, respectively.

The high-temperature reservoir is at the core of the RTG where a radioactive fuel stack radiates to a surrounding array of collectors, called hot shoes. This assembly is shown on the left in Fig 1. Here, T_H is governed by the ability of the hot shoes to absorb the energy radiated by the fuel stack.

The cold-temperature boundary is at the exterior of the RTG housing, where excess energy is rejected to the surrounding ambient environment. The exterior of the RTG onboard NASA's Perseverance mission is shown on the right in Fig 1, embedded in a protective mounting structure. Here, T_L is governed by the ability of the housing to reject heat to the surrounding environment. Because mission environments vary, so too does the extent to which radiation dominates heat rejection from the RTG. For missions whose environments eliminate all other modes of heat transfer, radiation is vital to model for accurate predictions of mission performance. However, this paper investigates only the interior, leaving the exterior for future work.



Figure 1: A stack of 3 GPHS Bricks surrounded by hot shoes and thermoelectric legs (left) and the Perseverance mission RTG with exposed radiative fins [2] (right)

Given that both the hot- and cold-side regions are dominated by radiation, it follows that an accurate model for the power output of an RTG must include an accurate model for radiation. The governing equation for radiative heat transfer between two bodies can be expressed as follows in Eqn 2 [3]

$$\dot{Q}_{1 \rightarrow 2} = \sigma A_1 F_{1 \rightarrow 2} (T_1^4 - T_2^4) \quad (2)$$

where σ is the Stefan-Boltzmann constant, A_1 is the total surface area of the emitting body, T_1 and T_2 are the temperatures of bodies 1 and 2, respectively, and $F_{1 \rightarrow 2}$ is the view factor from body 1 to body 2.

The view factor, $F_{1 \rightarrow 2}$, represents the fraction of energy emitted by body 1 that is coincident upon the surface of body 2. It is a geometrical factor, bounded on the closed domain $[0, 1]$. The analytic form of its solution, given below in Eqn 3, requires surface integration over the two participatory bodies, represented in Fig 2.

$$F_{1 \rightarrow 2} = \frac{1}{\pi A_1} \int_{A_1} \int_{A_2} \frac{\cos(\theta_1) \cos(\theta_2)}{r^2} dA_2 dA_1 \quad (3)$$

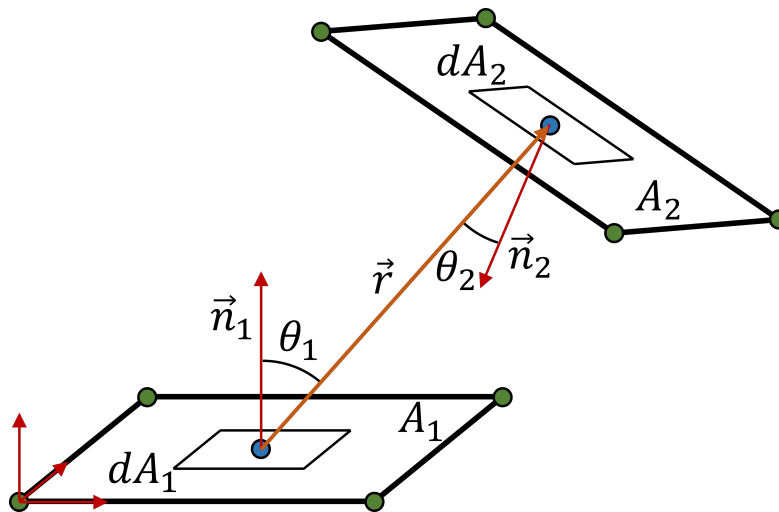


Figure 2: General F_{ij} Diagram

For real-world geometries, analytic integration of Eqn 3 is mathematically difficult, if even possible, so numerical integration is a practical necessity. There are numerous such schemes [4], but only Double Area Integration (DAI) and Single Area Integration (SAI), documented by NIST [4] have been implemented thus far in this project.

This work introduces the development of a novel numerical solver for the evaluation of benchmark-quality view factors between two arbitrary geometries. The DAI and SAI methods are explored, along with the effects of mesh refinement and integration quadrature on the accuracy of each numerical method relative to the analytic solutions to Eqn 3 for two benchmark geometries. Those techniques are then demonstrated in determining the view factors in the array of hot shoes for two different geometries of the central fuel stack. All RTG-related geometry was recreated according to the specifications laid out in the final Cassini mission report, which utilized a General Purpose Heat Source (GPHS) RTG [5].

1.1 Double Area Integration

The DAI scheme is a natural extension of the analytic form presented in Eqn 3 where the two surface integrals are discretized into summations, as shown in Eqn 4 [4].

$$F_{1 \rightarrow 2} = \frac{1}{\pi A_1} \sum_{A_i} \left[\sum_{A_j} \left[\frac{\cos \theta_1 \cos \theta_2}{r^2} \Delta A_j \right] \Delta A_i \right] \quad (4)$$

A_1 is the surface area of the emitting body. The angles θ_1 and θ_2 are formed between the surface normal vectors, \vec{n}_1 and \vec{n}_2 , and the ray cast between the differential elements, \vec{r} . The scalar $r = \|\vec{r}\|$. And ΔA_i and ΔA_j are the differential areas of the elements on the emitting and receiving bodies, respectively. Each of these is shown in Fig 2.

For computational efficiency gains, Eqn 4 is rewritten in the form of vector operations, as shown below in Eqn 5 [4].

$$F_{1 \rightarrow 2} = \frac{1}{\pi A_1} \sum_{A_i} \left[\sum_{A_j} \left[\frac{(\vec{r} \cdot \vec{n}_1)(\vec{r} \cdot \vec{n}_2)}{\|\vec{r}\|^3} \Delta A_j \right] \Delta A_i \right] \quad (5)$$

1.2 Single Area Integration

The SAI scheme was introduced by Hottel and Sarofim [6] for the view factor from a differential area dA_1 to a polygon A_2 , shown below. This transforms the area integral over A_2 into a series of line integrals over its edges, E_2 .

$$F_{1 \rightarrow 2} = \frac{1}{2\pi A_1} \int_{A_1} \sum_{j=1}^{E_2} [\vec{g}_j \cdot \vec{n}_1] dA_1 \quad (6)$$

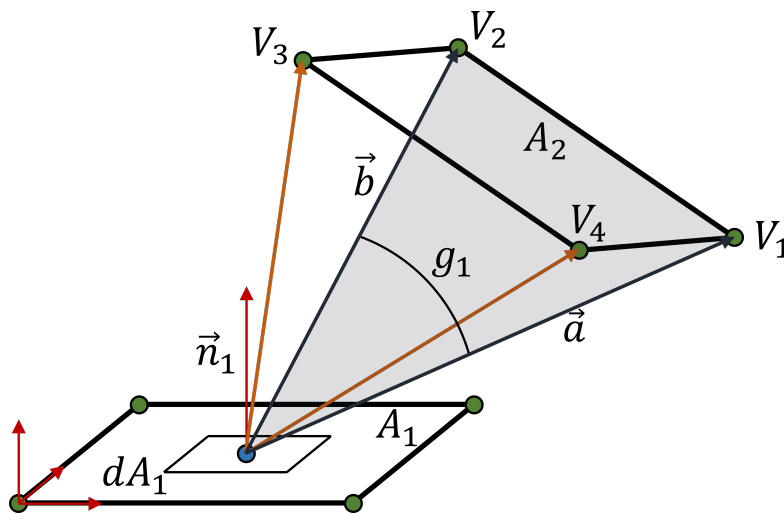


Figure 3: Relevant quantities in the SAI calculation

In Eqn 6, g_j is the magnitude of the angle subtended by \vec{a} and \vec{b} such that $\vec{g}_j \propto \vec{a} \times \vec{b}$ directs outwards from the enclosed volume formed between the centroid of the emitting element and the vertices of the

receiving element.

In the context of this solver, all differential areas are represented by triangular tessellation elements. As a result, the edges considered by the countour integral in Eqn 6 do not require contour discretization. By contrast, the DAI method relies upon discretization of both surfaces. It is because of this fact that, in practice, if the mesh of the receiving surface accurately captures its geometry, the value of $F_{1 \rightarrow 2}$ returned by SAI will, as will be demonstrated in later sections, be favorable for improved numerical accuracy over DAI.

The full discretized form of Eqn 6 is shown below in Eqn 7 [4].

$$F_{1 \rightarrow 2} = \frac{1}{2\pi A_1} \sum_{i=1}^{N^2} \left[\sum_{j=1}^{E_2} \left[\frac{\vec{c}_j \cdot \vec{n}_1}{e_j} \left[\frac{\pi}{2} - \tan^{-1} \left(\frac{d_j}{e_j} \right) \right] \right] \Delta A_i \right] \quad (7)$$

In this form, $\vec{c}_j = \vec{a}_j \times \vec{b}_j$, $e_j = \|\vec{c}_j\|$, and $d_j = \vec{a}_j \cdot \vec{b}_j$.

1.3 Techniques for Improving Numerical Accuracy

The process of domain discretization in numerical integration results in lower accuracy than the analytic equivalent. To combat this, mesh refinement and gaussian quadrature are implemented and studied to understand their standalone and combined effects on the numerical accuracy of both DAI and SAI.

1.3.1 Distmesh

Mesh refinement is accomplished using an iterative technique called `distmesh2d` [7]. This application utilizes MATLAB's implementation of the delaunayn triangulation algorithm. The vertices of the triangulation are iteratively shifted to minimize the structure's total strain energy, thereby producing relatively uniform-quality elements throughout the specified region.

The `distmesh2d` algorithm is adapted from the original research code for use specifically within the triangular regions of .STL meshes. An example triangular region between the vertices $(0, 0)$, $(1, 0)$, $(0, 1)$ is shown in Fig 4. The original element is highlighted by the black outline and the refined mesh produced by `distmesh2d` is shown in red.

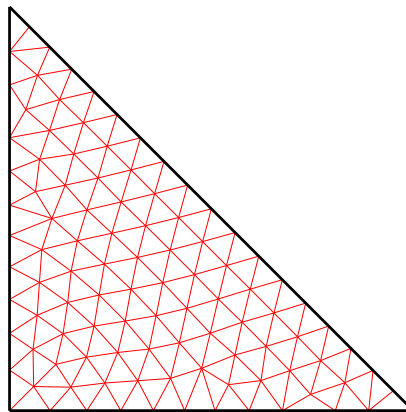
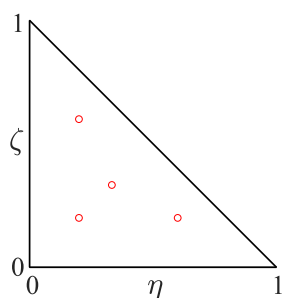


Figure 4: A triangular element (black) refined with `distmesh2d` [7] (red)

1.3.2 Quadrature

Gaussian integration, or quadrature, is a method by which numerical integration can be improved without the need for mesh refinement. In this context, rather than applying Eqns 5 & 7 only at the centroids of the emitting elements, they are applied at carefully selected integration points and combined via a weighted sum. The isoparametric coordinates, along with integration weights, as determined by Dr. John Burkardt for the STRANG3 method are tabulated as follows in Tab 1. This work only implements the STRANG3 method with four integration points, shown in Fig 5, but there are others of higher and lower order [8].



Weight	$-\frac{27}{48}$	$\frac{25}{48}$	$\frac{25}{48}$	$\frac{25}{48}$
η	$\frac{1}{3}$	$\frac{3}{5}$	$\frac{1}{5}$	$\frac{1}{5}$
ζ	$\frac{1}{3}$	$\frac{1}{5}$	$\frac{3}{5}$	$\frac{1}{5}$

Figure 5: An isoparameterized triangular element with the STRANG3 integration points [8] Table 1: Isoparametric coordinates for integration points and their associated weights [8]

2 Benchmark Geometries

The DAI and SAI algorithms were applied to the geometries of aligned parallel plates and aligned perpendicular plates with a common edge, both shown in Fig 6. These two configurations were chosen because analytic solutions to Eqn 3 do exist and because they are both very simple geometries, yet still prove challenging to handle numerically.

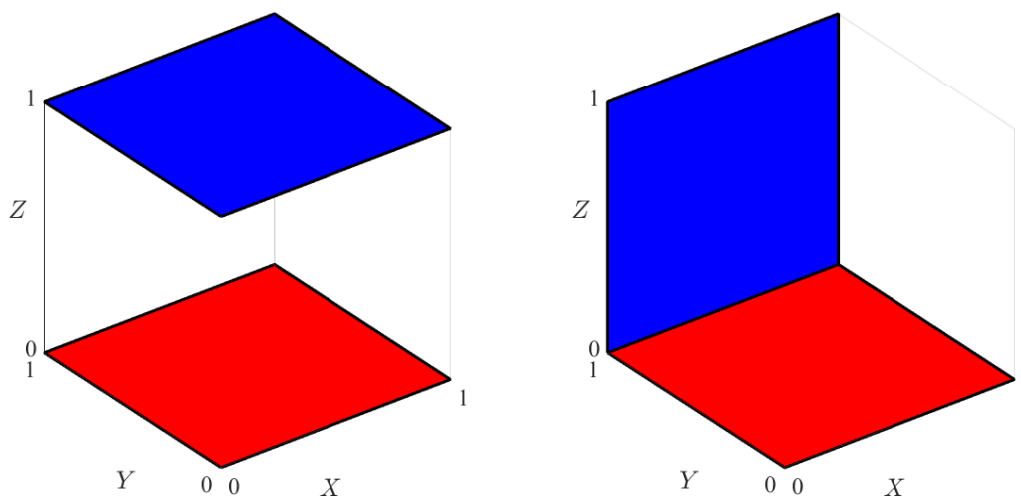


Figure 6: Aligned parallel plates (left) and aligned perpendicular plates (right)

2.1 Parallel Plates

Aligned parallel plates are configured as shown on the left in Fig 6. This image depicts two unit squares with a unit length separation between them. In general, this configuration is characterized by the quantities $\bar{X} = X/L$ and $\bar{Y} = Y/L$ where X is the length of the elements, Y is their depth, and L is

the distance separating them. The analytic solution to Eqn 3 for this configuration is given as follows in Eqn 8 [3].

$$F_{1 \rightarrow 2} = \left(\frac{2}{\pi \bar{X} \bar{Y}} \right) \left[\bar{X} \sqrt{B} \tan^{-1} \left(\frac{\bar{X}}{\sqrt{B}} \right) + \bar{Y} \sqrt{A} \tan^{-1} \left(\frac{\bar{Y}}{\sqrt{A}} \right) + \dots \right. \\ \left. \bar{X} \tan^{-1} (\bar{X}) + \bar{Y} \tan^{-1} (\bar{Y}) + \log \left(\sqrt{\frac{AB}{1 + \bar{X}^2 + \bar{Y}^2}} \right) \right] \quad (8)$$

$$A = 1 + \bar{X}^2, B = 1 + \bar{Y}^2$$

By varying the values of \bar{X} and \bar{Y} , a surface representing the value of $F_{1 \rightarrow 2}$ according to Eqn 8 is produced. For comparison, the surfaces produced by Eqns 5 and 7 are overlaid in Fig 7. Of particular note is the vertical scale for these graphs. DAI is observed to quickly exceed the bounds on $F_{1 \rightarrow 2}$ of $[0, 1]$. SAI, however, remains within these limits and qualitative comparison shows relatively good agreement with the analytic solution.

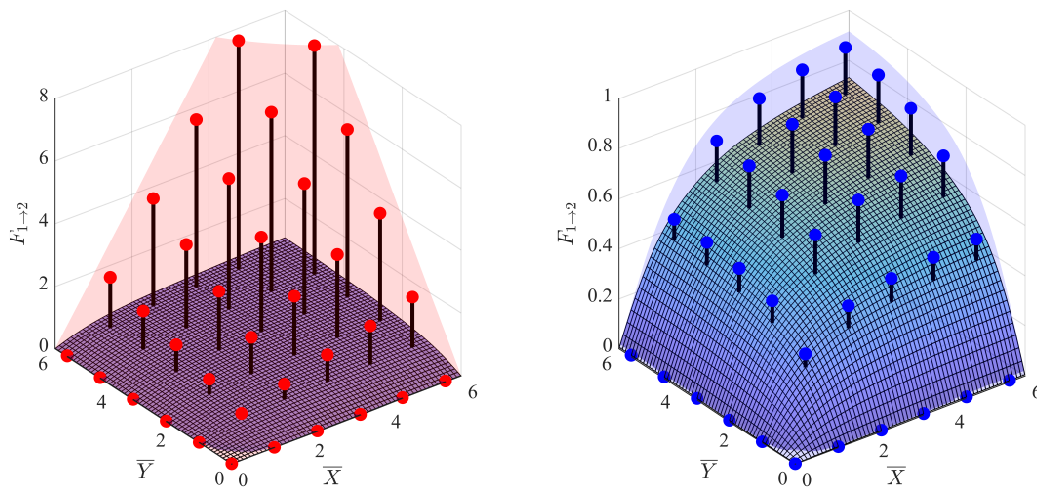


Figure 7: Comparison of DAI (left) and SAI (right) view factor calculations to the analytic model for parallel plates

This behavior from DAI demonstrates high sensitivity to relative separation [4], which is especially concerning in the broader context of this work in future applications for heat transfer. For any type of heat transfer solver, the possibility that $F_{1 \rightarrow 2}$ can exceed its physical limit is unacceptable as that would artificially inflate \dot{Q} from Eqn 2. Even before the application of mesh refinement and quadrature it is evident that SAI is a superior scheme to DAI.

2.2 Perpendicular Plates with a Shared Edge

Aligned perpendicular plates with a shared edge are configured as shown on the right in Fig 6. This image depicts two perpendicular unit squares with a common edge along the x-axis. In general, this configuration is characterized by the quantities $W = Y/X$ and $H = Z/X$ where X is the length of the common edge, Y is the depth of surface 1, and Z is the height of surface 2. The analytic solution to Eqn 3 for this configuration is given as follows in Eqn 9 [3].

$$F_{1 \rightarrow 2} = \frac{1}{\pi W} \left[W \tan^{-1} \left(\frac{1}{W} \right) + H \tan^{-1} \left(\frac{1}{H} \right) - D \tan^{-1} \left(\frac{1}{D} \right) + \dots \right. \\ \left. \frac{1}{4} \log \left(\left(\frac{AB}{C} \right) \left(W^2 \frac{C}{AD^2} \right)^{W^2} \left(H^2 \frac{C}{BD^2} \right)^{H^2} \right) \right] \quad (9)$$

$$A = 1 + W^2, B = 1 + H^2, C = 1 + W^2 + H^2, D = \sqrt{H^2 - W^2}$$

By varying the values of W and H , a surface representing the value of $F_{1 \rightarrow 2}$ according to Eqn 9 is produced. For comparison, the surfaces produced by Eqns 5 and 7 are overlaid in Fig 8. Similar to Fig 7, DAI is observed to quickly exceed the bounds on $F_{1 \rightarrow 2}$ of $[0, 1]$. Qualitatively, the surface generated by DAI also differs greatly from the analytic solution. SAI, however, remains within these limits and qualitative comparison shows relatively good agreement with the analytic solution.

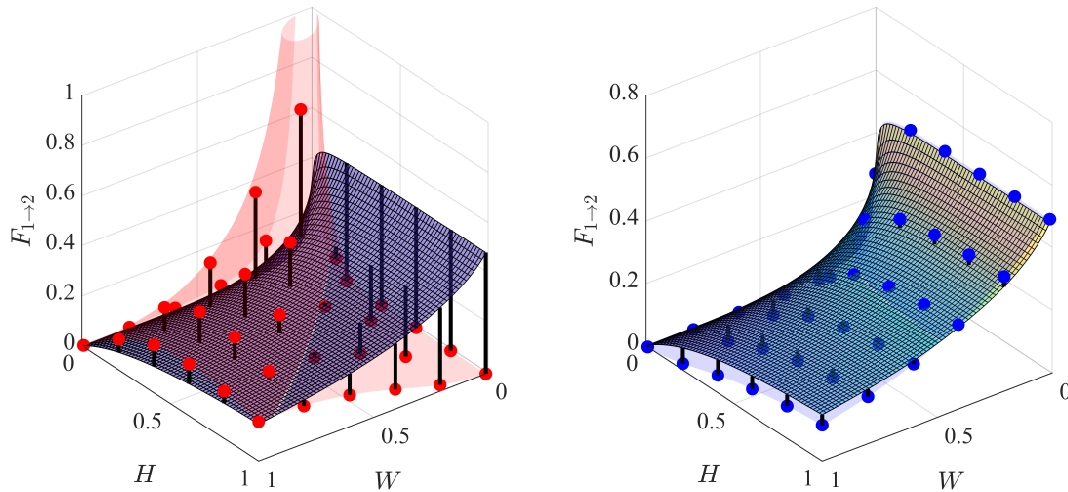


Figure 8: Comparison of DAI (left) and SAI (right) view factor calculations to the analytic model for perpendicular plates

2.3 Mesh Refinement

As discussed previously, the `distmesh2d` algorithm was used to refine the base meshes representing each of the benchmark geometries. For both configurations, the base mesh of each surface is represented by two triangular tessellations. Mesh refinement was applied at varying scale factors, for which the error of each numerical method was calculated with respect to the solutions to Eqns 8 and 9. The error was calculated as follows in Eqn 10.

$$E = \left| \frac{\text{numeric} - \text{analytic}}{\text{analytic}} \right| \quad (10)$$

It is expected that the application of `distmesh2d` will decrease the error for both DAI and SAI. When refining both the emitting and receiving meshes, this is indeed the result, as shown in Fig 9.

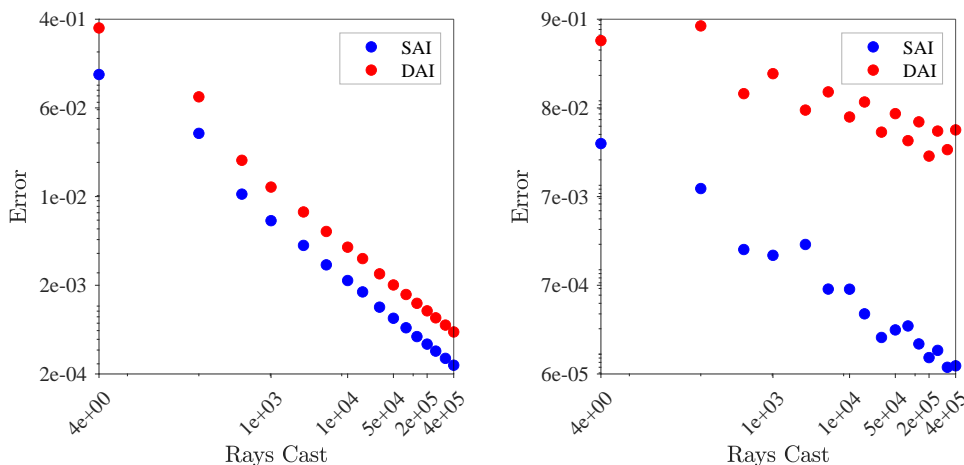


Figure 9: Error for DAI and SAI for parallel plates (left) and perpendicular plates (right) with refinement of both surfaces

Notably, while both DAI and SAI do converge towards the analytic solution, SAI achieves better accuracy. And it is clear that sensitivity to relative separation [4] is higher for perpendicular plates for both numeric methods. As the surfaces are refined, elements close to the common edge are increasingly problematic according to this metric. Despite this, SAI achieves even greater accuracy than for parallel plates, while DAI does not.

However, the true advantage of SAI arises with the refinement of only one surface. As a result of the discussion in Section 1.2, any discretization of the receiving surface beyond the initial input mesh has no effect on the numeric accuracy of SAI. This is demonstrated in Fig 10, where only the receiving surface is refined.

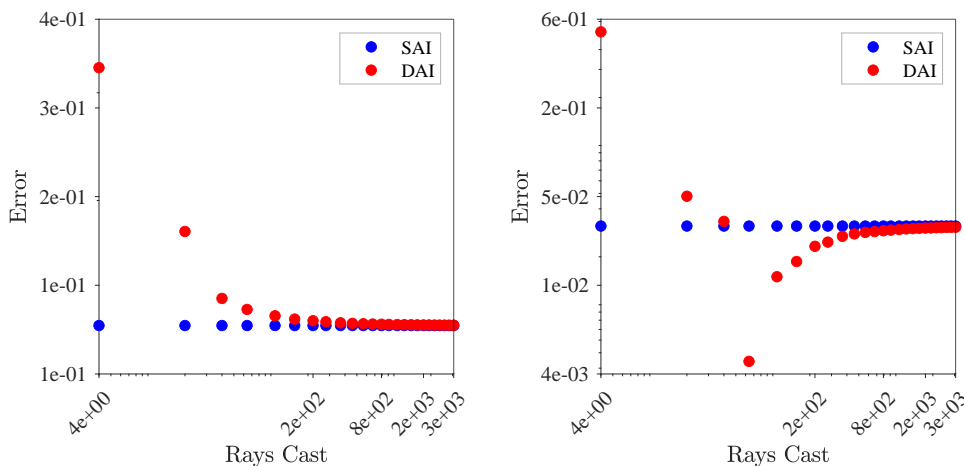


Figure 10: Error for DAI and SAI for parallel plates (left) and perpendicular plates (right) with refinement of the receiving surface

In this case, SAI does not change at all. DAI does vary, but it converges towards the value returned by SAI, instead of the analytic solution. This is because refinement of only one surface for DAI effectively approximates the method employed by SAI anyway. From this it can be determined that DAI requires the refinement of both participatory surfaces to converge towards the true solution.

When only the emitting surface is refined, DAI exhibits the same behavior as in Fig 10. However, unlike in Fig 10, the behavior of SAI matches that seen in Fig 9, converging towards the analytic

solution. These effects are demonstrated in Fig 11.

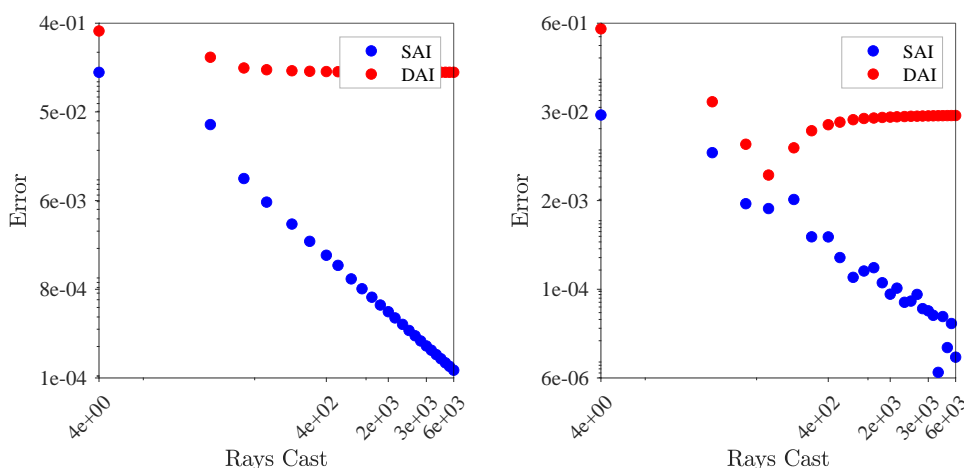


Figure 11: Error for DAI and SAI for parallel plates (left) and perpendicular plates (right) with refinement of the emitting surface

This result is particularly interesting because not only does SAI have the advantage prior to any mesh refinement, but it also only requires that one of the two participatory bodies be refined. In Eqns 5 and 7, it can clearly be seen that increasing the number of elements on either surface increases the number of computations that must be performed. So, the ability to resolve high-accuracy $F_{1 \rightarrow 2}$ results with only the need for refining the emitting surface poses the possibility for immense improvements in computation time. This lays the groundwork for future work that investigates the extent to which this is the case, if at all.

2.4 Quadrature

Building from the results in Fig 11, the application of quadrature further improves numerical accuracy, as seen in Fig 12.

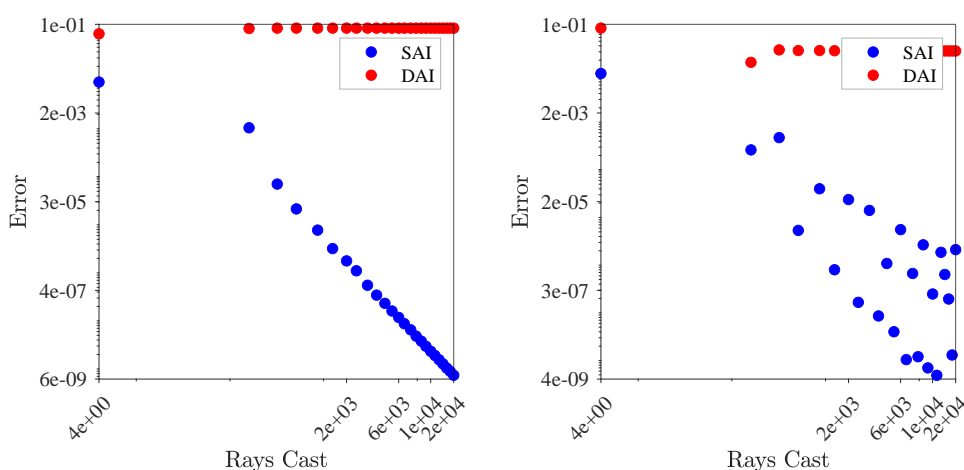


Figure 12: Error for DAI and SAI for parallel plates (left) and perpendicular plates (right) with refinement of the emitting surface and Gaussian Integration

For parallel plates, a dramatic decrease in error by five orders of magnitude is observed for SAI. For perpendicular plates, the results are again highly sensitive to relative separation. As seen, the error sometimes drops as low as three or four orders of magnitude below that seen without quadrature. But

the variability ultimately makes it difficult to take full advantage of this improvement for perpendicular plates.

It is important to note that the number of rays cast, which correspond to the number of calculations performed, does increase when gaussian integration is utilized. This work lays the foundation for future work benchmarking the changes in numeric accuracy and computation time that arise from the use of gaussian integration.

3 Application to RTG Hot Shoes

The hot shoes inside of the RTG are each positioned differently relative to the central fuel stack, which naturally leads to the conclusion that they each have a different view factor to the fuel stack. Because the view factor is a crucial piece in determining their temperatures, this work presents the values of $F_{1 \rightarrow 2}$ for each of the hot shoes in the array surrounding the GPHS RTG used in the Cassini mission.

3.1 Mesh Generation

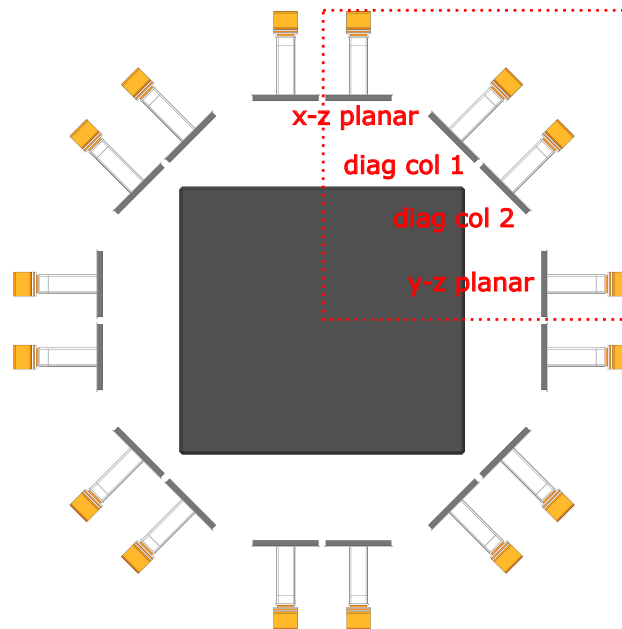


Figure 13: Top-down view of the hot shoe assembly around the central fuel stack with labeled columns

Each of the 72 meshes for the hot shoes was generated using `distmesh2d` within a square region of edge length 0.9 [in] located at the positions of each hot shoe in the array. Only 72 meshes were necessary because the total stack, 36 rows tall, is symmetric about its midpoint and the array exhibits $1/4$ symmetry around the longitudinal axis of the fuel stack, as shown in Fig 13. Therefore, 18 meshes were generated in 4 columns each, denoted the 'x-z planar', 'diag col 1', 'diag col 2', and 'y-z planar' columns, labeled in Fig 13. These correspond to their positions relative to the central fuel stack. The x- and y-dimensions of each brick in the central fuel stack are defined by a width $W = 3.92$ [in], a depth $D = 3.668$ [in], respectively. Refer to Fig 13 for their placements.

There are two different variations of the bricks in the central fuel stack: STEP1 and STEP2. The STEP1 geometry has 18 GPHS bricks, each with a height of $H = 2.09$ [in] stacked on top of each other, so that the total height of the central fuel stack is $H_{\text{tot}} = 37.62$ [in]. The STEP2 geometry has

16 GPHS bricks, each with a height of $H = 2.29$ [in], so that the total height of the central fuel stack is $H_{tot} = 36.64$ [in]. Both configurations are centered vertically with the hot shoe array.

The meshes for the bricks were also generated using `distmed2d` to represent the two faces that have a view of the hot shoes being considered. This was done to avoid unnecessary computation and to eliminate the extraneous features on each of the bricks, which serve only to increase mesh complexity without meaningfully affecting the overall geometry.

4 Results and Discussion

4.1 STEP1 Geometry

The results for the view factors from each of the hot shoes in the array to the two relevant faces of the fuel stack for STEP1 geometry are shown in Fig 14. Their index in the array is shown along the x-axis, starting with 1 at the top of the column along the axial direction and 18 in the center of the overall stack.

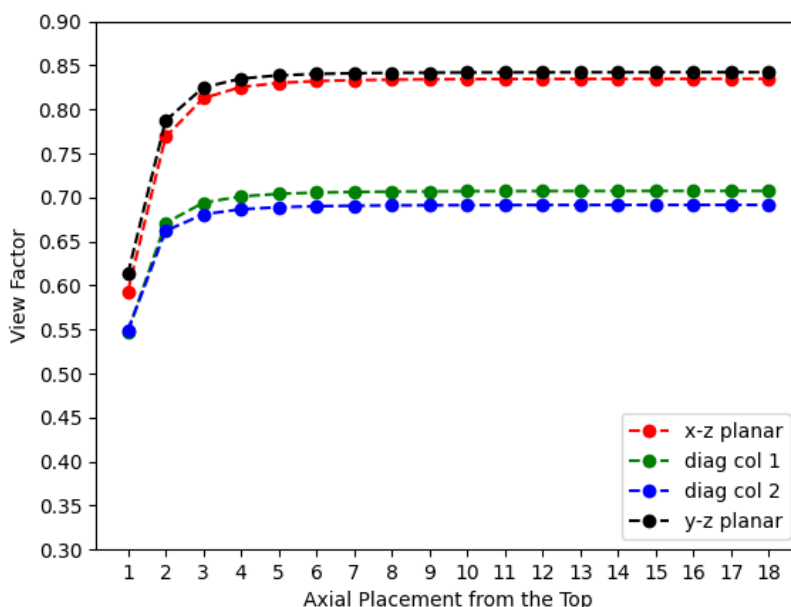


Figure 14: $F_{1 \rightarrow 2}$ for each of the hot shoes in the stack to the central fuel stack with STEP1 geometry

There is a clear drop in $F_{1 \rightarrow 2}$ for the columns along the diagonal of the GPHS bricks. This is an intuitive conclusion from the geometry of the surfaces relative to one another. It is also noted that for all four columns, hot shoes 1 and 2 have a lower view factor than the rest of their respective column. The combination of these findings indicates that the power delivery of the thermoelectric generator is nonuniform across the entire array. Not only are the hot shoes at the tops and bottoms of each column receiving less energy relative to the rest of their column, but a full half of the columns perform significantly worse than the other half because they are oriented towards the corner of the fuel stack.

4.2 STEP2 Geometry

These findings are replicated and even worsened, in the case of the top row, for the STEP2 geometry of the GPHS bricks. In Fig 15 it is seen that because the central fuel stack is approximately 1 [in] shorter, the hot shoes in the top and bottom rows experience a severe drop in the view factors to the fuel stack.

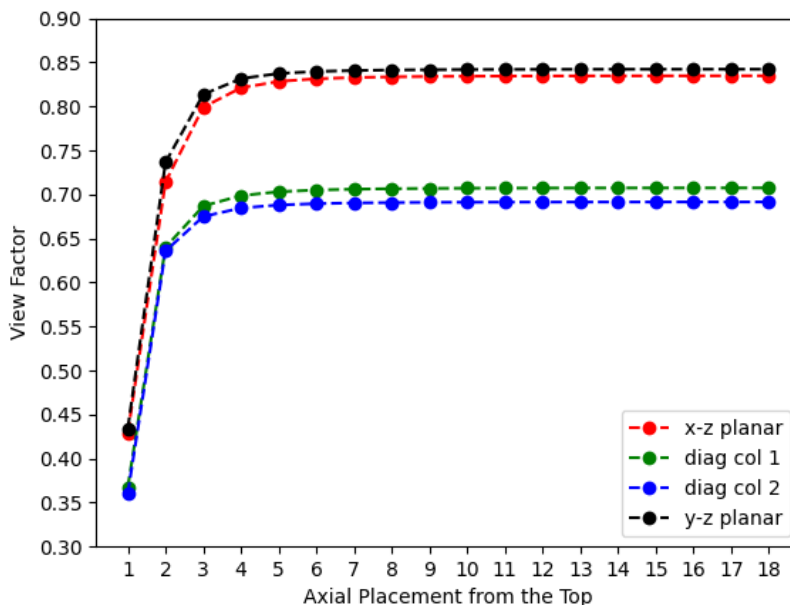


Figure 15: $F_{1 \rightarrow 2}$ for each of the hot shoes in the stack to the central fuel stack with STEP2 geometry

For the STEP2 geometry, it can be concluded that the top and bottom rows perform worse than for the STEP1 geometry. These results will inform future investigation into the extent to which the thermoelectric array is affected by placement relative to the fuel stack and along the longitudinal axis.

5 Conclusions

This study lays a strong theoretical and practical foundation for the implementation of Single Area Integration as the numerical method of choice in the development of a robust solver for evaluating view factors between two arbitrary bodies. The effects of mesh refinement and gaussian integration were demonstrated for parallel and perpendicular plates benchmark geometries, both shown to dramatically improve numerical accuracy for the two numerical methods investigated.

To demonstrate the application of this work for real-world value, the view factors for the hot shoe array were demonstrated relative to two different variations of the internal GPHS bricks in the central fuel stack. It was shown that the hot shoes in the top and bottom rows receive significantly less radiation from the fuel stack than the remaining rows. And importantly, it highlighted that the columns in the hot shoe array which face the corner of the fuel stack are handicapped relative to the columns which face the faces of the fuel stack.

This work sets the stage for future investigation into the characterization of the extent to which mesh refinement should be done in order to avoid both inaccurate results and unnecessary computation. Additionally, future work can determine the extent to which SAI improves computational runtime by eliminating the need for mesh refinement on the receiving surface and implementing gaussian integration. Finally, the view factor of the external RTG housing to its surroundings will be determined to evaluate how well it can reject heat from the system.

References

- [1] “Transit iv-a,” 1961.
- [2] “Perseverance looks back at wheel tracks,” 2010.
- [3] M. N. Özisik, *Heat Transfer A Basic Approach*. McGraw-Hill Book Company, 1985.
- [4] G. N. Walton, *Calculation of obstructed view factors by adaptive integration*. National Institute of Standards and Technology, Technology Administration, US Department of Commerce, 2002.
- [5] “Gphs-rtgs in support of the cassini rtg program. final technical report, january 11, 1991–april 30, 1998,” 8 1998.
- [6] H. C. Hottel and A. F. Sarofim, *Radiative Transfer*. McGraw-Hill Book Company, 1967.
- [7] P.-O. Persson and G. Strang, “A simple mesh generator in matlab,” *SIAM review*, vol. 46, no. 2, pp. 329–345, 2004.
- [8] “Quadrature_rules.tri quadrature rules for triangles,” 2010.